Delft University of Technology

Investigation of microstructure and oxidation properties of amorphous and nanocrystalline HfNbTaTiZr high-entropy alloy thin films

Hruška, Petr; Eijt, Stephan W.H.; Schut, Henk; Lukáč, František; Čížek, Jakub; Chevalier, Joris More; Cichoň, Stanislav; Vondráček, Martin; Fekete, Ladislav; More Authors

DOI
10.1016/j.surfcoat.2024.131642

Publication date
2025

Document Version
Final published version

Published in
Surface and Coatings Technology

Citation (APA)
Hruška, P., Eijt, S. W. H., Schut, H., Lukáč, F., Čížek, J., Chevalier, J. M., Cichoň, S., Vondráček, M., Fekete, L., & More Authors (2025). Investigation of microstructure and oxidation properties of amorphous and nanocrystalline HfNbTaTiZr high-entropy alloy thin films. *Surface and Coatings Technology*, *496*, Article 131642. https://doi.org/10.1016/j.surfcoat.2024.131642

Important note
To cite this publication, please use the final published version (if applicable).
Please check the document version above.

Copyright
Other than for strictly personal use, it is not permitted to download, forward or distribute the text or part of it, without the consent of the author(s) and/or copyright holder(s), unless the work is under an open content license such as Creative Commons.

Takedown policy
Please contact us and provide details if you believe this document breaches copyrights.
We will remove access to the work immediately and investigate your claim.

This work is downloaded from Delft University of Technology.
For technical reasons the number of authors shown on this cover page is limited to a maximum of 10.

Green Open Access added to TU Delft Institutional Repository

'You share, we take care!' - Taverne project

https://www.openaccess.nl/en/you-share-we-take-care

Otherwise as indicated in the copyright section: the publisher
is the copyright holder of this work and the author uses the
Dutch legislation to make this work public.

Surface & Coatings Technology 496 (2025) 131642

Contents lists available at ScienceDirect

Surface & Coatings Technology

journal homepage: www.elsevier.com/locate/surfcoat

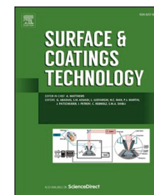

Investigation of microstructure and oxidation properties of amorphous and nanocrystalline HfNbTaTiZr high-entropy alloy thin films

Petr Hruška [a,b,*], Stephan W.H. Eijt [c], Henk Schut [c], František Lukáč [b,d], Jakub Čížek [b], Joris More Chevalier [a], Stanislav Cichoň [a], Martin Vondráček [a], Ladislav Fekete [a], Dejan Prokop [a,b], Ján Lančok [a]

[a] Institute of Physics of the Czech Academy of Sciences, Na Slovance 2, CZ 182 00 Prague, Czech Republic
[b] Charles University, Faculty of Mathematics and Physics, V Holešovičkách 2, CZ 180 00 Prague, Czech Republic
[c] Delft University of Technology, Faculty of Applied Sciences, Department of Radiation Science & Technology, Mekelweg 15, NL-2629, JB, Delft, Netherlands
[d] Institute of Plasma Physics of the Czech Academy of Sciences, Za Slovankou 3, CZ 182 00 Prague, Czech Republic

ARTICLE INFO

Keywords:
High-entropy alloys
Thin films
Defects
Positron annihilation spectroscopy
X-ray photoelectron spectroscopy

ABSTRACT

In this study, the deposition, annealing process, and oxidation properties of HfNbTaTiZr high-entropy alloy thin films were thoroughly investigated. The films, approximately 250 nm thick, were deposited on MgO substrates by DC magnetron sputtering using a single target. The preparation temperature was identified as a key factor influencing the resulting structure. Amorphous films formed at room temperature, whereas nanocrystalline films, characterized by multiple intermetallic phases, were obtained either by deposition at elevated temperatures (600 °C – 750 °C) or through *in situ* annealing of amorphous films (600 °C – 700 °C). Positron annihilation spectroscopy revealed that nanocrystalline films predominantly contain vacancy-like misfit defects, with concentration decreasing as the preparation temperature increases. Additionally, amorphous films exhibited a high concentration of large vacancy clusters. X-ray photoelectron spectroscopy showed greater oxygen absorption in amorphous films due to their defective structure, with preferential oxidation of Zr and Hf. Further annealing of naturally oxidized films in a vacuum at temperatures up to 1400 °C led to films' recrystallization and eventually the formation of complex oxides, including ZrO_2, HfO_2, and various Mg-containing oxides, indicating a reaction with the MgO substrate. This work demonstrates the ability to fine-tune the microstructure and defect characteristics of high-entropy alloy films and highlights their direct correlation with oxidation properties.

1. Introduction

The first successful demonstration of high-entropy alloys (HEAs) and HEA thin films 20 years ago [1,2] paved a new path for the development of new classes of materials based on these complex multi-principal element materials, including metallic alloys, oxides, carbides, and nitrides. HEAs typically consist of at least five principal elements, each with concentrations ranging from 5 to 35 at. % [3]. The original concept stems from the idea that a high number of constituents ensures a high configurational entropy of random solid solution (SS), significantly reducing the Gibbs free energy. This reduction stabilizes the random SS at the expense of a mixture of ordered intermetallic phases [3]. However, most current studies report on compositionally complex multiphase HEAs rather than true single-phase HEAs [4]. In addition to the slow self-diffusion in HEAs [5], presence of lattice distortions [3,6,7] results in a unique open-volume distribution and defect structures [8] compared to traditional metals and alloys.

Both bulk HEAs and HEA films have been intensively investigated due to their design flexibility and superior properties, such as mechanical properties [6,9–12], corrosion resistance [10,12–15], oxidation properties [16–18], electrical [19,20] and superconductive properties [21], hydrogen absorption capacity [22,23], and irradiation resistance [24,25]. Compared to the casting of bulk HEAs [26] [27], the deposition of thin films offers excellent flexibility in varying composition, microstructure, and morphology. This flexibility can be achieved relatively easily by adjusting deposition parameters to create amorphous films [10,11,28–32], characterized by a short- to medium-range-ordered structure with a high concentration of nanoscopic pores [16], or (nano)crystalline films [19,20,33–37], characterized by single or multiphase grains of the size from ∼10 to ∼100 nm in size. While the

* Corresponding author at: Institute of Physics of the Czech Academy of Sciences, Na Slovance 2, CZ 182 00 Prague, Czech Republic.
E-mail address: hruskap@fzu.cz (P. Hruška).

https://doi.org/10.1016/j.surfcoat.2024.131642
Received 16 September 2024; Received in revised form 4 December 2024; Accepted 6 December 2024
Available online 9 December 2024
0257-8972/© 2024 Elsevier B.V. All rights reserved, including those for text and data mining, AI training, and similar technologies.

effect of defects on the physical properties of bulk HEAs has been scarcely studied [38–40], their influence on the mechanical, electrical, and other properties of HEA coatings is yet to be fully investigated and understood.

Several approaches have been employed in the production of HEA coatings [10], with the most common methods being magnetron sputtering (MS) [10,11,25,28], pulsed laser deposition (PLD) [10,16,25,33,35,37,41], laser cladding [42], spraying processes [43], and electrodeposition [44]. Among these, MS and PLD are dominant due to the high quality of the resulting films. The potential of HEA thin films has been extended to the preparation of high-entropy ceramics (HEC) [45], such as high-entropy oxides, nitrides, carbides, silicides, and chalcogenides, by tuning the target compositions [41], through reactive deposition [30,31] or by electrochemical oxidation [46]. Given the wide selection of deposition techniques, understanding the influence of defects on the physical properties of the coatings is highly relevant, especially since PLD and MS have vastly different growth regimes.

Numerous HEA groups have been thoroughly investigated so far [4]. Among them, the refractory HEAs, which consist of refractory metals such as W, Mo, Ta, Nb, V, Hf, Zr, or Ti [3], exhibit a single-phase random SS with a bcc structure, which can be quenched and remains metastable at ambient temperature [26,27,47]. Within the multitude of HEA configurations, HfNbTaTiZr stands out as a member of the refractory materials group with a high melting point, thermal stability [17], and enhanced ductility and strength [48]. The casting of this alloy often results in a dendritic structure, and subsequent homogenization annealing produces large grains, making the alloy susceptible to embrittlement from absorbed atmospheric impurities [49]. Additionally, lattice distortions leading to a distribution of interstitial sizes [3] can positively influence the forming of an open structure favorable for hydrogen absorption [22,23]. HfNbTaTiZr thin films with variable thicknesses were prepared by DC magnetron sputtering under various growth conditions. It has been shown that HEAs grown at room temperature (RT) favor the formation of an amorphous structure [50,51]. The effects of deposition rate and substrate temperature on the film composition and structural properties were previously reported in [52–54].

Oxidation properties of refractory HEAs have been thoroughly investigated by Backman [55–57]. The surface oxidation of several HEA films has been investigated using X-ray photoelectron spectroscopy (XPS) combined with depth profiling [16,35]. Typically, a protective passivation layer [13,58–60] forms when these films are exposed to different corrosion environments. These layers exhibit diverse structures, ranging from disordered amorphous formations [15] to those displaying elemental segregation [13] or transitioning into a mixture of complex oxides [58]. Additionally, high-temperature oxidation behavior [15,58,61] remains a significant research challenge for HEAs. Detailed information regarding the nature of lattice defects and the quantification of oxidation properties in both crystalline and amorphous structures is crucial for understanding the link between defects and the oxidation properties of HEA films.

In the preliminary experiment, building upon the results of the previous study [16], we subjected the amorphous HfNbTaTiZr film, which had naturally oxidized due to prolonged exposure to ambient air, to annealing under a vacuum of 10^{-7} Pa. The annealing temperature gradually increased up to 700 °C. Instead of crystallization, the formation of ZrO_2 and HfO_2 nanoparticles was observed by X-ray diffraction (XRD), presumably due to the chemisorbed oxygen inside the film volume [16]. In this paper, we report on how deposition parameters intricately influence the microstructure of HfNbTaTiZr films. We investigate two different annealing routes and demonstrate that the microstructure, including both crystalline phases and defect structures, can be effectively tuned by varying deposition conditions.

The defect structure of HfNbTaTiZr films was investigated using positron annihilation spectroscopy (PAS) with a variable-energy positron beam (VEP). Thermalized positrons implanted into the material undergo diffusion and can either annihilate in a delocalized state as free positrons or become trapped in open-volume defects, which act as potential wells confining the positron wave function. PAS is renowned for its exceptional sensitivity to open-volume defects [62,63] as well as can provide valuable insights into the interstitial regions and local chemical order within HEAs, a significant experimental challenge in this field [64]. In this work, Doppler broadening analysis – a PAS method that examines the momentum distribution of electrons at the annihilation site – was employed. The broadening of the annihilation line, caused by a non-zero momenta of annihilating pair, is usually characterized by two line-shape parameters S and W. The low-momentum S parameter is particularly sensitive to defects, increasing with defect concentration and size, while the W parameter carries information on the local chemical environment of defects, provided by high-momentum core electrons. Depth-resolved analysis of S and W parameters measured as a function of positron implantation energy was performed using the VEPFIT code [65,66] offering a detailed characterization of the open-volume defects within the studied films.

The natural oxidation of the HfNbTaTiZr films was investigated by XPS, revealing a stronger susceptibility to oxidation in amorphous and nanocrystalline films containing large vacancy clusters. *In situ* VEP monitoring described the artificial oxidation of films gradually annealed up to 1400 °C, confirming our preliminary studies.

2. Experimental

HfNbTaTiZr films were deposited by DC magnetron sputtering in an ultra-high vacuum (UHV) deposition chamber [16]. The DC power supply operated at 10 W, and the magnetron discharge was maintained in an Ar atmosphere at a constant pressure of 2 Pa, regulated by a needle valve to ensure a fixed Ar flow of 14 sccm. Table 1 details the deposition conditions for 6 films deposited on single crystal MgO (100) substrates with dimensions 10×10 mm^2. Three fabrication routes were defined: (i) deposition at RT resulting in an amorphous film [16]; *in situ* annealing at a temperature T_{ann}, without exposure to ambient atmosphere, of the film deposited at RT for 1 h; (iii) deposition on the substrate kept at the high temperature (HT) T_{dep}. A single 20 mm diameter HfNbTaTiZr target, utilized for all depositions, was prepared by spark plasma sintering (SPS) at 1000 °C for 15 min under 100 MPa pressure, using gas-atomized powder of the HfNbTaTiZr alloy [27]. Film thicknesses were determined using a KLA Tencor P-6 Stylus Profiler, and the deposition time for all films was 60 min.

X-ray diffraction (XRD) measurements were conducted using a Bruker Discover diffractometer equipped with a 1D LynxEye. Asymmetric Bragg-Brentano θ-2θ geometry with a 1.5° angle of deviation, Cu-Kα radiation (wavelength of 1.54051 Å), and 2θ angles ranging from 5°

Table 1
Deposition conditions of HfNbTaTiZr films: base pressure p_0, DC voltage U and current I, deposition temperature T_{dep}, and annealing temperature T_{ann}. Films' thicknesses obtained by profilometry and corresponding deposition rates are included.

Sample	p_0 (Pa)	U (V)	I (mA)	T_{dep} (°C)	T_{ann} (°C)	Thickness (nm)	Dep. rate (nm/min)
D-020	4×10^{-8}	223	44.8	20	–	248(7)	4.1(1)
A-600	3×10^{-7}	218	45.9	20	600	237(7)	4.0(1)
A-700	5×10^{-8}	220	45.5	20	700	234(7)	3.9(1)
D-600	8×10^{-9}	228	43.8	600	–	263(8)	4.4(1)
D-700	2×10^{-8}	232	43.1	700	–	272(7)	4.5(1)
D-750	1×10^{-6}	236	42.4	750	–	284(6)	4.7(1)

to 150°, were employed. The Rietveld refinement analysis of XRD patterns was performed using the TOPAS V5 code [67], assuming that small crystallites and microstrains contribute to broadening of Lorentzian and Gaussian components of pseudo-Voigt function, respectively. CALPHAD modelling was used to describe the temperature-dependent evolution of the crystalline phases for the HfNbTaTiZr system using the TCHEA7.0 software [68].

The surface morphologies of the films were characterized using atomic force microscopy (AFM). AFM measurements were carried out at room temperature on an ambient AFM Bruker Dimension Icon in Peak Force Tapping mode with ScanAsyst Air tips with $k = 0.4$ N/m and nominal tip radius 2 nm. The measured topographies had dimensions of 5×5 μm^2 and 1×1 μm^2 with a resolution of 512×512 points.

X-ray Photoelectron Spectroscopy (XPS) analysis was performed in the Omicron NanoESCA instrument, operating in a vacuum of 10^{-8} Pa or better, and utilizing a monochromatized Al Kα radiation source ($h\nu =$ 1486.7 eV). Under these conditions, the information depth is limited to a few nanometers. Spectral fitting and interpretation were performed using CasaXPS and KolXPD software. Elemental quantification was carried out employing Scofield's Relative Sensitivity Factors, as provided in CasaXPS. No corrections were applied to the instrument transmission function nor the photoelectron inelastic mean free path.

A series of experiments employing vacuum transport directly to the XPS apparatus was conducted to investigate short-term oxidation in HfNbTaTiZr films. Additional samples with thicknesses of approximately 100 nm were prepared specifically for XPS measurements under the same deposition conditions as used for the D-20, D-600, and D-750 samples, detailed in Table 1. The vacuum transport constituted a UHV vacuum suitcase (10^{-7} Pa) connected to the deposition chamber and maintained by an ion pump operating at 100 nA. The freshly prepared films were transferred to the suitcase immediately after deposition. Once detached, the suitcase was brought directly to the XPS instrument for immediate analysis. Standard samples, which had been exposed to the atmosphere for approximately 20 min, were used for comparison.

For the analysis of subsurface regions, depth profiling of the samples was enabled by an Ar^+ ion sputter gun in the preparation chamber of the NanoESCA instrument, with the sputtering conditions set at E = 3 keV, pressure 2×10^{-4} Pa, and normal incidence angle. 1 min of depth profiling removes approximately 0.5 nm of the film thickness.

The proportions of metallic, suboxide, and oxide contributions of individual elements were determined through semi-quantitative analysis. Binding energy calibration and charge correction followed the method outlined here. Nb and Ta exhibited relatively large metallic contributions due to their lower reactivity. To ensure accurate calibration, we shifted the peaks for Nb^0 (Nb $3d_{5/2} = 202.5$ eV) and Ta^0 (Ta $4f_{7/2} = 22.2$ eV) to match literature-reported values [69,70]. This approach was preferred over calibration based on adventitious carbon contamination, as no carbon was present in the vacuum-transported samples, and also carbon was removed after the initial depth profiling step. The peak shift was typically no larger than a few tenths of an eV.

Positron annihilation spectroscopy (PAS) was conducted using a continuous variable energy slow positron beam (VEP) operating at Delft University of Technology [71]. The incident positron energies were varied within the range of 0.1 to 24.5 keV, corresponding to mean implantation depths from the surface up to 670 nm calculated from the Makhovian distribution [72] using the HfNbTaTiZr bulk density of 9.94 g/cm^3 [26]. Energy spectra E_γ of annihilation photons were collected by a single High-Purity Germanium (HPGe) detector.

Doppler broadening $\Delta E = E_\gamma - m_0c^2$ of the annihilation peak at 511 keV (the rest energy of electron/positron), caused by a non-zero momentum of the annihilating pair, was characterized by two line-shape parameters S and W [72]. The low momentum shape S parameter is defined as the relative surface area of the central part of the peak with an energy window of $|\Delta E| < 0.77$ keV, or alternatively, electron momentum $|p| < 3.0 \times 10^{-3}$ m_0c. The high momentum wing W parameter is defined as the relative surface area within the energy window of 2 keV $< |\Delta E| < 6$ keV, or corresponding electron momentum 8.2×10^{-3} m_0c $< |p| < 23.4 \times 10^{-3}$ m_0c. The S parameter is particularly sensitive to open-volume defects, where the probability of annihilation with valence electrons is enhanced. Conversely, the W parameter reflects annihilation events with core electrons, providing insight into the chemical environment of the annihilation site. Measuring S and W parameters as a function of implantation energy E of the positron beam enables us to obtain depth-resolved information about defects in studied thin films. The resulting S(E) and W(E) curves were analyzed by the VEPFIT code [65,66], which numerically solves a positron diffusion equation for a layered structure, using Makhovian positron implantation profiles.

3. Results and discussion

3.1. Morphology and structural analysis

The effect of deposition temperature and post-deposition *in situ* annealing on the microstructure of HfNbTaTiZr films, in particular their morphology, can be visualized by AFM measurements, as shown in Fig. 1. The figure displays AFM scans with detailed insets with higher magnification. Additionally, the root mean squared roughness R_q is provided for each scan. In Fig. 1a, the film deposited at RT exhibits a morphology consistent with previously reported amorphous films deposited on fused silica substrates [16], featuring characteristic round-shaped granular nanostructures approximately 10 nm in diameter. Alongside this smooth appearance ($R_q = 1.7$ nm), regularly shaped formations, likely oxide nanoparticles of ~100 nm size, are present on top of the film. A detailed 0.5×0.5 μm^2 view of 2 such nanoparticles is depicted in Fig. 1a. XRD showed no coherent diffraction from these nanoparticles particularly due to their small size and small volume fraction.

In situ annealing of the amorphous film led to the transformation and development of well-defined nanostructures of ~100 nm in size, as illustrated in Fig. 1b and Fig. 1c. Regularly shaped formations remain present on the surface. The morphology of annealed films is similar for both annealing temperatures of 600 °C and 700 °C ($R_q = 7.9$ nm for both films), with the higher annealing temperature promoting the growth of larger nanostructures on average. Fig. 1d-f showcase three distinct morphologies of films deposited at HT, characterized by larger, well-oriented nanostructures (≥ 100 nm) compared to annealed films. The film deposited at 600 °C exhibits a square-like morphology ($R_q = 13.0$ nm), which gradually transitions into a "maze-like" structure, characterized by interconnected grains, at 700 °C ($R_q = 13.8$ nm), and further evolves at 750 °C ($R_q = 11.4$ nm).

Additional information about the crystalline structure can be obtained from the XRD results, presented in Fig. 2. The broad peak (□) at ~43°, observed consistently across all films, corresponds to the residuum of MgO (100) single-crystal substrate diffraction, which is effectively suppressed by the chosen asymmetric measurement geometry. For the film deposited at RT, no distinct diffraction peaks are observed. Instead, a broad peak (○) typical for metallic glasses appears at 36.8° (FWHM 4.3°), suggesting the presence of an amorphous structure, consistent with prior findings [16,50]. The center of this peak corresponds to an average nearest-neighbor distance of 2.44 Å, closely resembling the (110) interplanar distance of 2.41 Å in the high-entropy bcc2 phase [27], where it is equal to the nearest-neighbor distance. The diffraction coherence length, calculated from the Lorentzian fit, is determined to be 1.6(1) nm. Such a value corresponds to the medium-range order in metallic glasses [73].

The growth of thin films is governed by the surface diffusion of deposited atoms. At lower temperatures, significant variations in atomic sizes, (Table S1 in Supplementary Information), lead to sluggish diffusion, reaching a critical point where the formation of a long-range-ordered crystalline phase is hindered. When the temperature is increased to 600 °C or higher – implemented either by post-deposition annealing or elevated deposition temperature – atomic diffusion

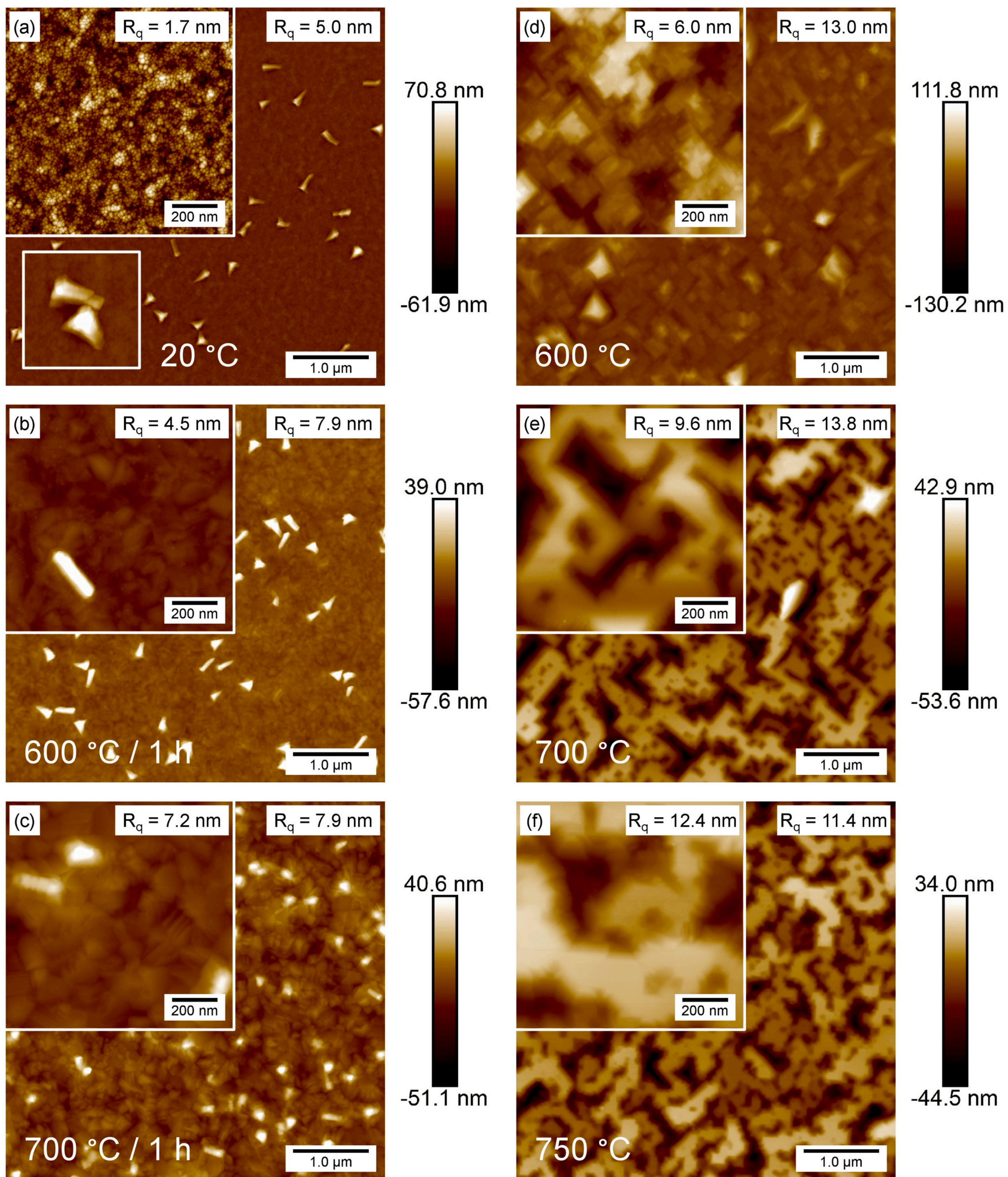

Fig. 1. AFM 5 × 5 μm^2 scans with detail 1 × 1 μm^2 insets: (a) D-20 (RT deposition), (b) A-600 (RT deposition +600 °C / 1 h annealing), (c) A-700 (RT deposition +700 °C / 1 h annealing), (d) D-600 (600 °C deposition), (e) D-700 (700 °C deposition), (f) D-750 (750 °C deposition). The surface roughness R$_q$ is depicted in the top right corner of each scan.

accelerates enough to facilitate the development of crystalline structures. As shown in Fig. 2, XRD patterns reveal notable differences between films that crystallized through *in situ* annealing and those deposited directly at HT. In the case of post-deposition annealing, the amorphous film crystallizes as atoms rearrange throughout the film volume (post-deposition crystallization). In contrast, during HT deposition, the crystalline structure develops progressively at the elevated temperature (in-deposition crystallization).

In situ annealed films (A-600 and A-700) exhibit two distinct crystalline phases: hcp (*) and bcc1 (×). The bcc1 phase shows a unit cell parameter of 3.335–3.339 Å, which is much less than the expected 3.408 Å for the equimolar HfNbTaTiZr composition [27]. This suggests that the bcc1 phase has been depleted by larger atomic radius elements such as Hf and Zr. In contrast, the hcp phase displays lattice parameters

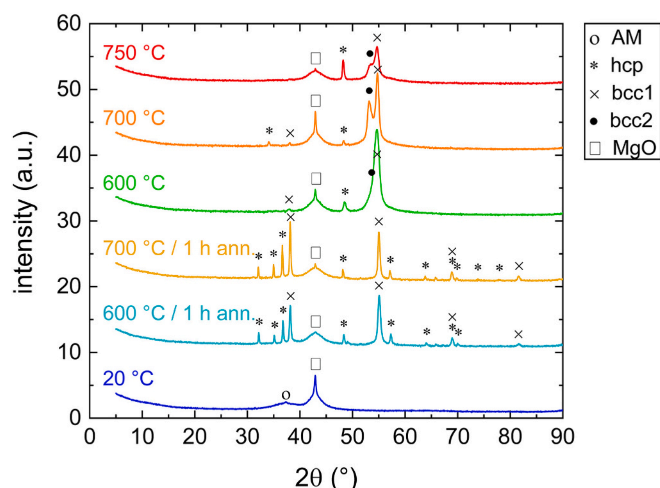

Fig. 2. XRD patterns for HfNbTaTiZr films deposited at various temperatures (T_{dep} = 20 °C, 600 °C, 700 °C, 750 °C) or annealed *in situ* (T_{dep} = 20 °C, T_{ann} = 600 °C, 700 °C). Peaks from amorphous (AM), hcp, bcc1, and bcc2 phases as well as the residual signal from MgO substrate are labeled.

indicative of a composition dominated by a mixture of Hf and Zr. Consequently, post-deposition crystallization results in a multiphase films with a Hf,Zr-rich hcp phase and a Nb,Ta-rich bcc1 phase. Lattice parameters obtained from Rietveld analysis are included in Table S1 (Supplementary Information). These observations align with our CALPHAD modelling shown in Fig. S1 (Supplementary Information) and is consistent with a previous study of the HfNbTaTiZr system [47]. However, as detailed in [47], the exact compositions of the phases vary with the temperature and cannot be determined here.

No strong texture was observed in the annealed films. In contrast, the films deposited directly at HT displayed a distinct behavior. The strong texture observed in these films is consistent with AFM observations, revealing large, well-oriented grains and enhanced roughness. A relatively small signal from hcp phase was observed, with dominant $(10\overline{1}1)$ and $(10\overline{1}2)$ reflections, while the majority of the films is presumed to consist of highly textured bcc structures. The dominant (200) peak is split into two peaks, which can be interpreted as the formation of two phases: the bcc1 phase, with lattice parameter of 3.347–3.358 Å, and the bcc2 phase with a unit cell parameter >3.408 Å. This indicates that the bcc1 phase is still enriched with elements of smaller atomic radius, such as Nb and Ta, while the bcc2 phase must be enriched in larger elements, like Zr and Hf, since the lattice parameter of the bcc2 phase exceeds that of the equimolar composition. This Hf,Zr-enriched bcc2 phase has also been observed in the temperature range of 700–1000 °C, as reported in previous studies [47].

Consequently, post-deposition and in-deposition crystallizations lead to different outcomes. The phase composition of the annealed films appears closer to thermodynamic equilibrium, with the atomic diffusion activated throughout the whole film volume. For the films grown directly at HT, however, surface diffusion plays a crucial role, resulting predominantly in highly textured bcc phases, that differ from the equilibrium state at the given temperature.

3.2. Defect structure

The microstructural variability of HfNbTaTiZr films at the atomic scale can be effectively explored through defect studies. Positron annihilation spectroscopy (PAS) using a variable-energy positron beam VEP serves as an excellent tool for investigating defects in thin films [71]. Reference measurements were conducted on two HfNbTaTiZr targets: before the deposition (target #1) and after the deposition (target #2) as well as on the bare MgO substrate (Fig. S2 in Supplementary Information). Positron lifetime spectroscopy studies on bulk HfNbTaTiZr alloy prepared by SPS [27] identified small vacancy-like misfit defects as the dominant defect component, alongside a minor fraction of free positrons that were not trapped by defects. Therefore, the reference S parameter of 0.511, observed for pristine target #1, can be attributed to the low-defective bulk HfNbTaTiZr alloy. In contrast, the reference S parameter of 0.558, observed for target #2 damaged by Ar^+ sputtering, represents a highly defective state with increased concentration of vacancy clusters and voids. The reference S parameter for the MgO substrate was determined as 0.461.

The S parameters of HfNbTaTiZr films are plotted as a function of positron energy (E) in Fig. 3. The thermalization of monoenergetic positrons implanted in the material follows the Makhovian implantation profile[1] [72]. Depending on positron energy and the corresponding implantation depth, three distinct regions of positron annihilation are resembled: the surface, the film, and the substrate. Transitions between these regions occur due to the diffusion of thermalized positrons among them and broadening of the implantation profile with increasing positron energy. At lower energies (E < 2–5 keV), positrons primarily annihilate on the surface as epithermal and thermal positrons. As the energy increases (2–5 keV < E < 13 keV), positrons penetrate deeper, leading to an increasing fraction of annihilations inside the film, accompanied by a rising S parameter. The S parameter for all HfNbTaTiZr films falls within the interval defined by the reference values of targets #1 and #2. At higher energies (E > 13 keV), positrons predominantly annihilate in the MgO substrate. Fractions of positrons annihilating on the surface, in the film, and in the substrate, as modelled by VEPFIT [65,66], are illustrated in Fig. S3 (Supplementary Information).

The behavior of W(E) function is qualitatively opposite to S(E).

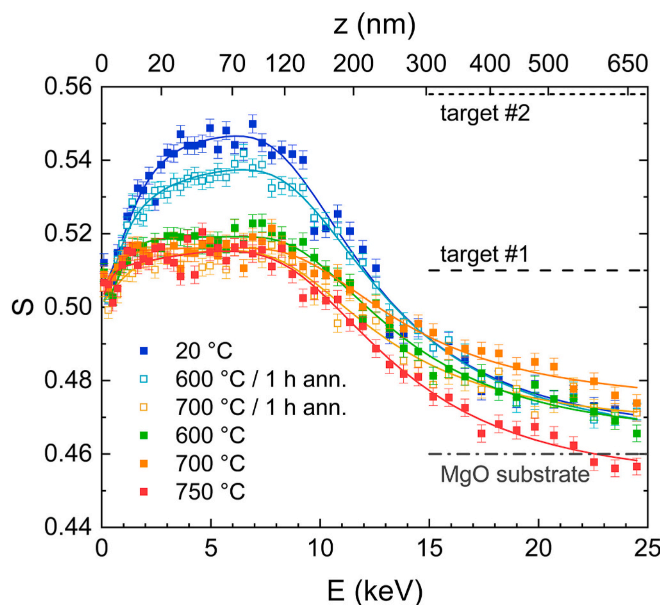

Fig. 3. S(E) plots of HfNbTaTiZr films. Reference S values for the HfNbTaTiZr target #1 and #2, and the MgO substrate are included. Solid lines are model curves calculated by VEPFIT. The mean positron implantation depth in HfNbTaTiZr alloy is depicted on the top axis.

[1] Makhovian profile is defined as $f(z,E) = \pi\frac{z}{2\overline{z}^2}exp\left[-\pi\left(\frac{z}{2\overline{z}}\right)^2\right]$, where $\overline{z} = \frac{40}{\varrho}E^{1.6}$ is the mean implantation depth. The interval $\left(\frac{1}{2}\overline{z}, \frac{3}{2}\overline{z}\right)$ contains 68 % of implanted positrons.

Additional insight into distinct positron annihilation states is provided by plotting both parameters in the so-called S-W plot, shown in Fig. 4. In this plot, the small data points (open squares) represent the measured S and W values, while the large points obtained from VEPFIT, corresponding to the idealized scenario where 100 % of the positrons annihilate in a particular state (surface, film, or substrate). The surface data points are located in the central part for all films. The S and W parameters of the films (illustrated as full squares) reside in the bottom-right corner, while the substrate data points, including the reference S and W value (depicted as an open circle), are positioned in the top-left corner. The measured data points follow linear lines between surface-film and film-substrate S and W values, indicating a gradual transition as positrons penetrate deeper into the material. These linear trends suggest a uniform distribution of defects throughout the entire volume of the film where the concentration of vacancy-like misfit defects and vacancy clusters remains constant across the film thickness. The linear dependence of S—W data points reflects variations in the fractions of positrons annihilating in the different regions (surface, film, or substrate) with increasing positron energy, while the S and W parameters for each region remain constant.

One can see in Fig. 3 and Fig. 4, that the S parameter of the D-20 film, deposited at RT, is substantially higher than that of the other films. In the prior study [16], two types of defects were identified in the amorphous film by positron lifetime spectroscopy: vacancy-like misfit defects (relative intensity of 80 %) situated between amorphous clusters, and large vacancy clusters (relative intensity of 20 %). Comparison with the reference target #2 (depicted as a black circle in Fig. 4), which shows a higher S value but comparable W value, indicates a higher concentration and/or larger mean size of vacancy clusters, possibly accompanied by larger pores, in the ion-bombarded bulk compared to the amorphous film.

The D-600, D-700, and D-750 films show S and W values similar to those of the reference target #1 (depicted as a filled grey circle in Fig. 4). The slightly lower S value for target #1 likely results from the contribution of annihilations of free positrons [27], characterized by a lower S parameter than annihilations of positrons trapped in defects. This suggests that, compared to the reference target #1, nanocrystalline films

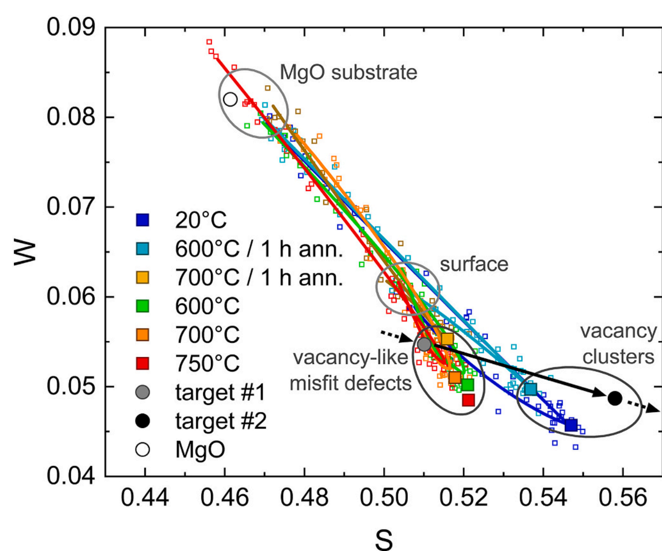

Fig. 4. S-W plot resembling the following regions: surface, HfNbTaTiZr films, and MgO substrate. Full squares represent S and W values for the films, while small data points (open squares) represent S and W parameters measured across different positron energies. Reference values for the bulk target (pristine – grey circle, damaged – black circle), and MgO substrate (open circle) are included. Solid lines are model curves calculated by VEPFIT. The black arrow indicates the transition from a defect-free structure to a film containing vacancy-like misfit defects and, ultimately, to a structure containing only vacancy clusters.

deposited at HT contain a higher concentration of vacancy-like misfit defects, which are common in such films due to atomic mismatches within the grain structure.

The defect structure of for the A-700 film, deposited at RT and subsequently annealed at 700 °C, closely resembles that of films deposited at HT, exhibiting similar S and W parameter values. This similarity indicates that vacancy clusters, originally present in the amorphous film, completely disappeared during crystallization at 700 °C. In contrast, the substantially higher S parameter of the A-600 film, annealed at a lower temperature of 600 °C, suggests it retains a significant concentration of vacancy clusters. Consequently, despite the nanocrystalline structure of the A-600 film, its defect structure partially resembles that of the amorphous D-20 film. Although the morphology and crystal structures of both annealed films are very similar, the higher annealing temperature of 700 °C enables greater atomic relocation, which, along with the growth of hcp and bcc1 crystallites, leads to the evolution of vacancy-like misfit defects and the recovery of the vacancy clusters, as observed by PAS. This comparison highlights that, regarding the reduction of vacancy clusters, in-deposition crystallization (films deposited at HT) proves to be more effective than post-deposition crystallization (*in situ* annealed films). The S and W values for all films follow a trend, illustrated by the black arrow in Fig. 4, indicating the progression from an ideal defect-free structure to that with vacancy-like misfit defects, and eventually to the structure containing only vacancy clusters.

By employing the VEPFIT code, we obtain the positron diffusion length L_+ in addition to the S and W values of the films. This parameter provides complementary information about the defect structure and is proportional to the positron trapping rate in defects. L_+ decreases with increasing defect concentration or average size [62], showing opposite behavior to the S parameter. However, L_+ is more sensitive to the concentration of defects, while the S parameter is more responsive to average defect size. The VEPFIT parameters for the HfNbTaTiZr layers are included in Table S2 (Supplementary Information) and graphically shown as a function of temperature in Fig. 5. Additionally, the concentrations (cv*) of vacancies in misfit defects and in vacancy clusters were roughly estimated using the formula detailed in the Supplementary Information.

Illustrations of three distinct microstructures (I., II., and III.), integrating our findings from XRD and PAS results, are included in Fig. 5. The amorphous structure (I.) exhibits the largest average defect size, with both vacancy-like misfit defects and vacancy clusters present in the highest concentration, as evidenced by the highest S parameter and the lowest L_+. Post-deposition annealing at 600 °C partially reduces the vacancy clusters, leading to a decrease in the average defect size, as indicated by the decrease in S. This results in a nanocrystalline structure (II.) with a defect concentration comparable to that of the amorphous structure, reflected by similarly low L_+ values. At a higher annealing temperature of 700 °C, vacancy clusters are almost entirely recovered, producing a nanocrystalline structure (III.) with minimal vacancy clusters. Although the concentration of misfit defects also decreases, it remains substantially higher – by an order of magnitude – than in films deposited at $T_{dep} \geq 700$ °C. Notably, as the deposition temperature increases, the misfit defect concentration drops rapidly, while the average defect sizes remain comparable. This trend aligns with the growth of crystallites at higher deposition temperatures, effectively reducing the volume fraction of phase interfaces and thus concentration of misfit defects.

3.3. Natural oxidation

Bulk target #1 (before the deposition) was characterized by XPS, with detailed results available in the Supplementary Information. The sample exhibited behavior reminiscent of non-evaporable getters (NEG): upon annealing at 500 °C for 30 min, hydrogen naturally absorbed at room temperature was released, while oxygen migrated from the surface

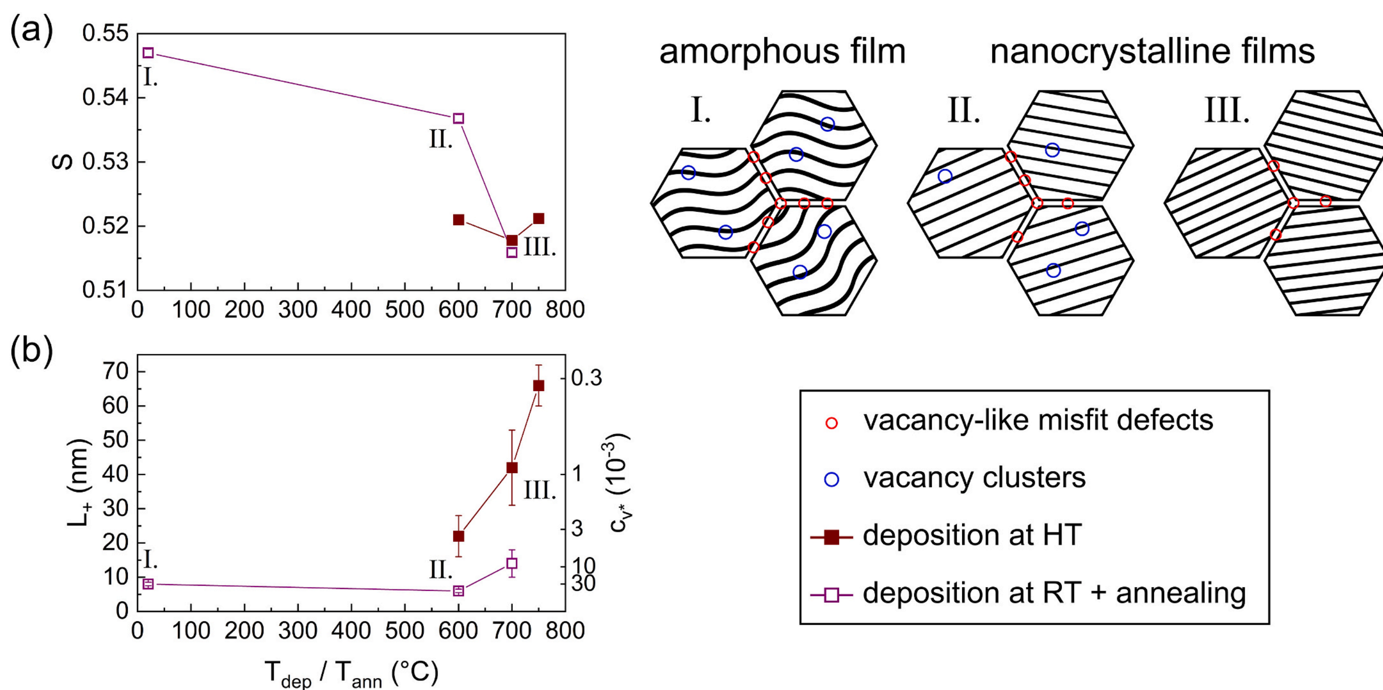

Fig. 5. VEPFIT parameters of HfNbTaTiZr layers: S parameter and positron diffusion length L_+, plotted as a function of the deposition temperature T_{dep} (full squares) or the annealing temperature T_{ann} (open squares). Solid lines serve as guides-to-the-eye for the temperature dependence of S and L_+ parameters. Three distinct microstructures were resolved and are illustrated in the figure: I. amorphous structure, II. nanocrystalline structure containing vacancy clusters, and III. nanocrystalline structure containing only vacancy-like misfit defects.

into the bulk. This NEG-like effect is likely inherent to the HfNbTaTiZr alloy composition, independent of microstructure.

The Group 4 elements in HfNbTaTiZr films are highly reactive, rapidly oxidizing upon exposure to ambient conditions [55,74]. Freshly deposited films undergo non-negligible reactions with the environment during transport to the XPS instrument, meaning conventional oxidation studies may overlook this critical early stage, potentially leading to an incomplete understanding of the overall process. To capture the effects of short-term natural oxidation of HfNbTaTiZr films, we compared vacuum-transported samples (kept in UHV at 10^{-7} Pa) with standard samples, exposed to ambient air during the transport to XPS apparatus.

XPS spectra after 15 min and 120 min depth profiling steps are presented in the Supplementary Information. Three types of films were compared: amorphous film deposited at RT, and nanocrystalline films deposited at 600 °C and 750 °C. The oxidation behavior of individual elements followed expected trends based on each element's position in the periodic table. Specifically, the affinity towards oxygen increases with atomic number and is higher for the Group 4 (Ti, Zr, Hf) compared to the Group 5 (Nb, Ta) [74,75].

The standard amorphous film showed the highest level of oxidation with dominant ZrO_2 and HfO_2 peaks, while Ti, Nb, and Ta are present in both metallic and oxide states. By further depth profiling, the Group 4 elements were partially reduced, while Nb and Ta were already in pure metallic state. In contrast, the vacuum-transported amorphous film and all nanocrystalline films exhibited predominantly metallic peaks of all elements for both depth profiling steps. The fast oxidation of the amorphous film in ambient air is attributed to its structure containing large vacancy clusters, confirming the authors' previous study [16]. Moreover, nanocrystalline films, containing only vacancy-like misfit defects, seem to be significantly less susceptible to natural oxidation.

Normalized atomic concentrations of metallic elements, obtained through XPS analysis of Ti 2p, Nb 3d, Zr 3d, Ta 4f, and Hf 4f core levels, correspond to an average value of 20 at. %, accounting for uncertainties associated with the XPS method [76]. These uncertainties are primarily due to common sputtering-associated parasitic effects [69,70] and material damage during depth profiling [77], such as preferential sputtering or reduction of distinct elements, leading to possible alterations in the sample composition. Concentrations of oxygen and carbon, obtained from O 1 s and C 1 s core levels, as functions of profiling time, are shown in Fig. 6 for the amorphous and nanocrystalline films, respectively.

After the initial profiling step of 15 min, a rapid decrease in oxygen concentration is observed in the vacuum-transported amorphous and both nanocrystalline films. In contrast, the standard amorphous film shows significant oxidation even within the bulk after extended profiling. The relatively high oxygen concentration in vacuum-transported films before the start of depth profiling can be attributed to the transport conditions, as complete avoidance of exposure to residual reactive gases is impractical when using the vacuum suitcase. This issue is particularly relevant for the reactive metals composing the films, highlighting the need for an ideal direct vacuum transfer. The benefits of purer vacuum transport conditions are evident, as the vacuum-transported nanocrystalline sample exhibits lower oxygen content compared to the standard sample. Additionally, the presence of carbon and higher oxygen content at the surface suggests the adsorption of light organics during the transport of standard samples.

At greater depths, both standard and vacuum-transported nanocrystalline films show similarly low oxygen proportions, as shown in Fig. 6b. Both films developed a thin oxidized layer, a few tens of nm thick, with the effect being more pronounced in the standard sample, which was exposed to the ambient atmosphere for a short period. In amorphous films, oxygen chemisorption is evident, as the standard film exhibits higher oxygen concentrations than the vacuum-transported counterpart. The observed oxygen concentrations may be elevated due to the high reactivity of the metals and sputtering-related effects during profiling. Nevertheless, the vacuum-transported samples still discernible oxygen presence in the bulk, implying that potential oxidation may have occurred even during deposition.

The XPS results indicate that nanocrystalline films with distinct phase structures exhibit higher resistance to short-term natural

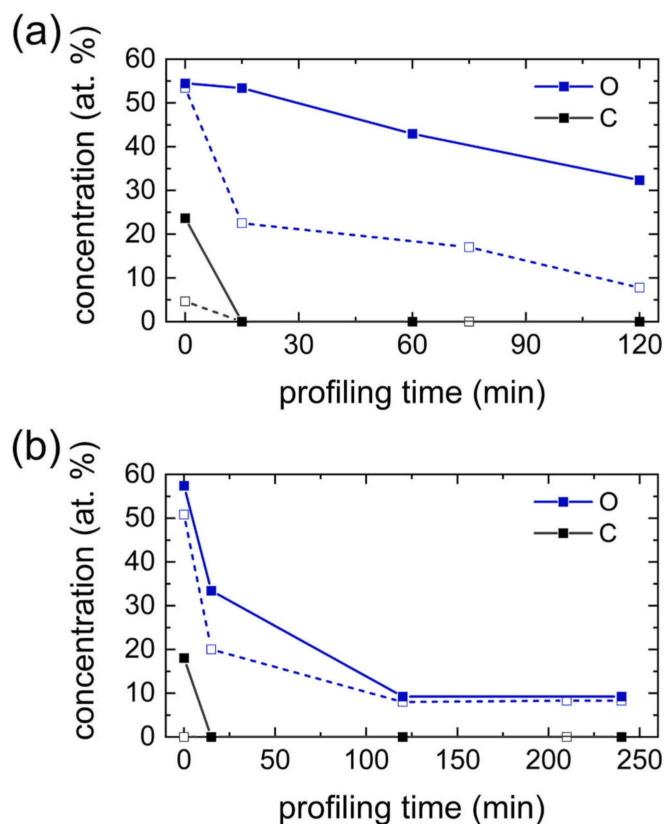

Fig. 6. Oxygen and carbon concentrations in: (a) amorphous films (T_{dep} = 20 °C) and (b) nanocrystalline films (T_{dep} = 600 °C) comparing standard samples (full points + full lines) and vacuum-transported samples (open points + dashed lines).

oxidation owing to their compact structure, characterized by vacancy-like defects as the dominant type of open-volume defect. In contrast, amorphous films, which contain large vacancy clusters, are more susceptible to oxygen absorption from the air.

3.4. *Artificial oxidation*

All films, with microstructures discussed in sections 3.1 and 3.2, were stored without protective atmosphere and exposed to air for extended period (typically ranging from several days to months) before being analyzed by AFM, XRD, and PAS. AFM observations revealed the possible presence of oxide nanoparticles on the surfaces of films deposited at RT. However, XRD patterns showed no evidence of coherent diffraction from oxides, apart from intermetallic phases. Additionally, the S(E) curves displayed no variations in the S parameter across the films, indicating the absence of an oxygen gradient.

The thermal stability of microstructures of three selected films: D-700 (T_{dep} = 700 °C), D-600 (T_{dep} = 600 °C), and D-20 (T_{dep} = 20 °C), was assessed through annealing experiments in the VEP vacuum apparatus. The experiments involved isochronal step-by-step annealing up to 1400 °C, accompanied by *in situ* VEP measurements. Each experiment spanned 6 days, with total 27 h of annealing. To prevent atmospheric contamination, the experiments were conducted under a vacuum pressure range of 10^{-6} to 10^{-3} Pa, which gradually increased as the annealing temperature rose.

Structural characterizations following the full annealing sequence revealed complete oxidation in all samples. A detailed description of the morphology, observed by AFM, and the crystalline structure, analyzed by XRD, is provided in the Supplementary information. All three annealed films exhibit similar structures, characterized by large grains exceeding 1 μm in size. Phase analysis identified the formation of ZrO_2 and HfO_2, along with complex oxides, containing Mg, resulting from the reaction between the film with MgO substrate at high temperatures.

In situ real-time VEP monitoring provides insight into the structural development during high-temperature artificial oxidation. Each annealing step (100 min) comprised: 1. a temperature rise and stabilization (30 min), 2. a single-energy measurement at elevated temperature (35 min), and 3. subsequent free cooling to RT (30 min). The temperature was increased by 100 °C per step, with additional data points at 650 °C and 750 °C. Due to the time-intensive nature of the experiment, the measurement was performed at the single positron energy of 6 keV, where the S parameter represent a superposition of two distinct states: annihilation of thermal positrons at the surface and the predominant annihilation within the HfNbTaTiZr layer, as shown in Fig. S3 in the Supplementary Information. Additionally, four full S(E) curves were measured at RT after 4 steps (T_{ann} = 400 °C), 8 or 9 steps (T_{ann} = 700 °C or 750 °C), 12 or 13 steps (T_{ann} = 1000 °C or 1100 °C), and 16 steps (T_{ann} = 1400 °C).

The evolution of the microstructure in the D-700 film with annealing temperature (T_{ann}) is displayed in Fig. 7. The S(T_{ann}) plot in Fig. 7b reveals three distinct temperature intervals. At low annealing temperatures (T_{ann} < 500 °C), S increases linearly with T_{ann} (I.) due to an increased S parameter of the surface, as apparent in Fig. 7d (T_{ann} = 400 °C). As observed by XPS in section 3.3, the NEG-like behavior of HfNbTaTiZr alloy, at these temperatures, especially at the surface, promotes hydrogen desorption from the surface and concurrent oxygen diffusion into the film volume. In nanocrystalline films, hydrogen atoms absorbed during prolonged air exposure are bound to vacancy-like defects [78,79]. During annealing (I.), hydrogen release from these defects effectively reduces electron density (of low momentum electrons) at the annihilation site and consequently increasing the S parameter, while the W parameter remains relatively unchanged, see Fig. 7c. Additionally, the S parameter decreases during the free cooling of the film (open points in Fig. 7b). This hydrogen desorption correlates with a rapid increase in the base pressure in the chamber during temperature rise, as shown in Fig. 7a. The temperature range up to 500 °C reflects the thermal stability of absorbed hydrogen. Notably, the possible formation of thermal vacancies would have a negligible effect on S parameter growth, as T_{ann} is too low and the film already contains a high concentration of vacancy-like misfit defects. Lattice thermal expansion can be also disregarded since most positrons annihilate in defects.

In the interval of medium annealing temperatures (500 °C < T_{ann} < 1000 °C), the S parameter remains nearly constant (II.), as shown Fig. 7b. Although phase transformations of intermetallics cannot be ruled out, the S parameter is relatively insensitive to different nanocrystalline phase structures, as demonstrated in section 3.2. At high annealing temperatures T_{ann} > 1000 °C, a significant decrease in S is observed, alongside an increase in base pressure (III.), as displayed in Fig. 7a,b, suggesting that bulk oxidation of the film occurs primarily above 1000 °C, likely with oxygen sourced from the MgO substrate. Furthermore, after annealing at the highest temperatures, both S and W parameters of the film approach the values characteristic of the MgO substrate, as shown in Fig. 7d,e., making differentiation from substrate values challenging. The D-600 film shows qualitatively similar behavior to the D-700 film, with analogous S(E), S—W, and S(T_{ann}) plots presented in the Supplementary Information. This trend can thus be generalized for nanocrystalline films deposited at HT.

Results for the initially amorphous D-20 film annealed up to 1400 °C are depicted in Fig. 8 and reveal the same three temperature intervals (I., II., and III.) as observed for the D-700 film. The pronounced increase in S at low annealing temperatures (T_{ann} < 500 °C) in Fig. 8b suggests greater hydrogen desorption, likely due to higher hydrogen content absorbed in the amorphous structure (I.). In the medium temperature range (500 °C < T_{ann} < 1000 °C), a notable decrease in the S parameter occurs without major changes in base pressure (Fig. 8a), which can therefore be attributed to film crystallization (II.), as supported by the

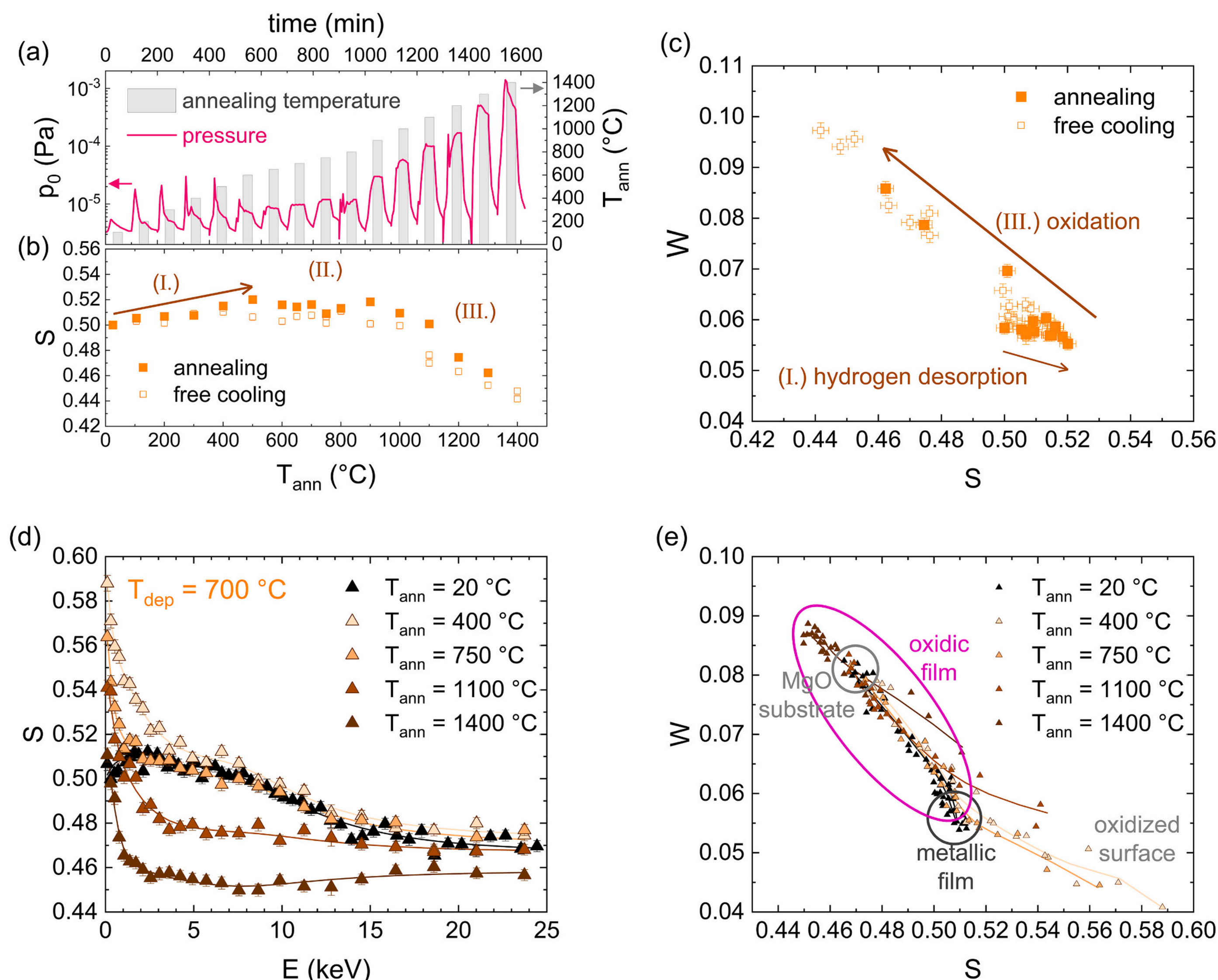

Fig. 7. D-700 film (T_{dep} = 700 °C) gradually annealed up to 1400 °C in VEP apparatus. (a) Time evolution of the base pressure p_0 and annealing temperature T_{ann}. (b) Temperature dependence of the single-energy S parameter S(T_{ann}). (c) S—W plot for the single-energy S and W parameters. (d) Full S(E) curves measured at selected annealing temperatures. (e) Corresponding S—W plots, with solid lines as model curves calculated by VEPFIT. Full data points represent measurement at elevated temperatures (annealing), open points represent measurements during free cooling in vacuum.

position of corresponding data points in the S—W plot in Fig. 8c. Presumably, ZrO_2 and HfO_2 phases were formed during this phase, as indicated by their higher intensities observed by XRD, facilitating naturally absorbed oxygen in the amorphous structure over an extended period. At high annealing temperatures (T_{ann} > 1000 °C), oxidation is indicated by a qualitatively similar drop in the S parameter as observed in the case of nanocrystalline films (III.), see Fig. 8b,c. In the final annealing step, the S(E) curves again display an indistinguishable transition from the film to the MgO substrate, as shown Fig. 8d,e.

Both the nanocrystalline and amorphous HfNbTaTiZr films exhibit thermal metastability, with common processes of hydrogen desorption at low annealing temperatures (T_{ann} < 500 °C) and artificial oxidation by reaction with the MgO substrate at high annealing temperatures (T_{ann} > 1000 °C) leading to the formation of crystallites of complex oxide phases. This shared behavior accounts for their similar morphology and phase structures, as confirmed by AFM and XRD. However, in the intermediate temperature range (500 °C < T_{ann} < 1000 °C), only the amorphous D-20 film exhibited artificial oxidation promoting the formation of ZrO_2 and HfO_2 by facilitating the relatively high concentration of naturally absorbed oxygen.

4. Conclusions

HfNbTaTiZr films were deposited on MgO substrates by DC magnetron sputtering, utilizing a single target fabricated through spark plasma sintering. Deposition at room temperature resulted in a medium-range ordered amorphous structure, while nanocrystalline films were produced either by deposition at high temperatures or by *in situ* post-deposition annealing of the amorphous films. Phase analysis revealed a multiple-phase structure, including hcp structure and 2 bcc structures. Positron annihilation spectroscopy identified a high concentration of vacancy clusters in the amorphous films. In contrast, nanocrystalline films deposited at high temperatures displayed vacancy-like misfit defects as the primary type of defect, with their concentration gradually decreasing as the deposition temperature increased. Crystallization of the amorphous films was accompanied by the recovery of vacancy clusters, which was more pronounced at higher annealing temperatures.

The role of defects in the natural oxidation properties under ambient atmosphere was investigated using X-ray photoelectron spectroscopy. While various nanocrystalline films demonstrated comparable oxygen absorption, limited to depths of a few tens of nanometers, the

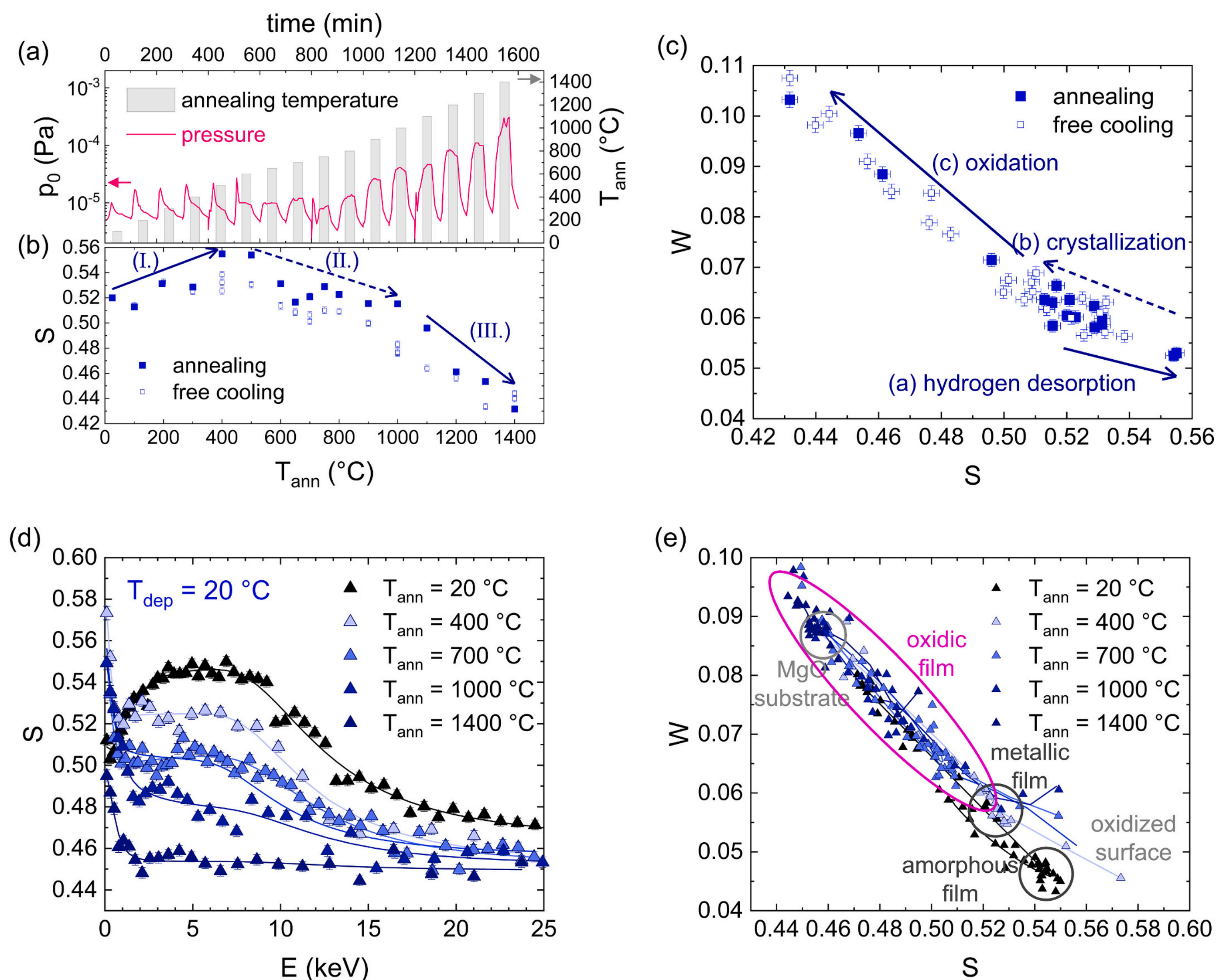

Fig. 8. D-20 film (T_{dep} = 20 °C) gradually annealed up to 1400 °C in VEP apparatus. (a) Time evolution of the base pressure p_0 and annealing temperature T_{ann}. (b) Temperature dependence of the single-energy S parameter S(T_{ann}). (c) S—W plot for the single-energy S and W parameters. (d) Full S(E) curves measured at selected annealing temperatures. (e) Corresponding S—W plots, with solid lines as model curves calculated by VEPFIT. Full data points represent measurement at elevated temperatures (annealing), open points represent measurements during free cooling in vacuum.

amorphous film exhibited a heightened susceptibility to oxygen absorption due to its defective structure. Furthermore, preferential oxidation Zr and Hf over Ti, Nb, and Ta was observed. The films also exhibited non-evaporable getter-like behavior, where hydrogen was released from the film during annealing, allowing absorbed oxygen to diffuse inward from the surface. Regardless of their initial structure, annealing the films in a vacuum at temperatures increasing up to 1400 °C led to recrystallization and the formation of complex oxide phases. This artificial oxidation resulted from the reaction between the film and the MgO substrate and the naturally absorbed oxygen within the film.

This study demonstrates that the microstructure and defect structures of high-entropy alloy films can be finely controlled, offering valuable insights into tailoring their properties, enhancing performance, and expanding potential applications. These findings lay the groundwork for future research and technological innovations in the field of high-entropy alloys.

CRediT authorship contribution statement

Petr Hruška: Writing – review & editing, Writing – original draft, Validation, Project administration, Investigation, Formal analysis, Conceptualization. **Stephan W.H. Eijt:** Writing – review & editing, Validation, Supervision, Methodology. **Henk Schut:** Supervision, Software, Methodology, Data curation. **František Lukáč:** Resources, Investigation, Formal analysis. **Jakub Čížek:** Writing – review & editing, Validation, Conceptualization. **Joris More Chevalier:** Resources, Investigation, Funding acquisition. **Stanislav Cichoň:** Writing – review & editing, Investigation, Formal analysis. **Martin Vondráček:** Investigation, Formal analysis. **Ladislav Fekete:** Investigation. **Dejan Prokop:** Investigation, Formal analysis. **Ján Lančok:** Resources, Project administration, Funding acquisition.

Declaration of competing interest

The authors declare that they have no known competing financial interests or personal relationships that could have appeared to influence the work reported in this paper.

Acknowledgments

This work was supported by the NATO grant SPS MYP G6153. J. More Chevalier acknowledges the support of the Czech Science Foundation (project 23-05002S).

Appendix A. Supplementary data

Supplementary data to this article can be found online at https://doi.org/10.1016/j.surfcoat.2024.131642.

Data availability

Data will be made available on request.

References

[1] J.-W. Yeh, et al., Formation of simple crystal structures in cu-co-Ni-Cr-Al-Fe-Ti-V alloys with multiprincipal metallic elements, Metall. Mater. Trans. A 35 (8) (2004) 2533–2536, https://doi.org/10.1007/s11661-006-0234-4.
[2] J.W. Yeh, et al., Nanostructured high-entropy alloys with multiple principal elements: novel alloy design concepts and outcomes, Adv. Eng. Mater. 6 (5) (2004) 299–303, https://doi.org/10.1002/adem.200300567.
[3] D.B. Miracle, O.N. Senkov, A critical review of high entropy alloys and related concepts, Acta Mater. 122 (2017) 448–511, https://doi.org/10.1016/j.actamat.2016.08.081.
[4] W. Steurer, Single-phase high-entropy alloys – a critical update, Mater. Charact. (2020) 162, https://doi.org/10.1016/j.matchar.2020.110179.
[5] M.-H. Tsai, J.-W. Yeh, High-entropy alloys: a critical review, Mater. Res. Lett. 2 (3) (2014) 107–123, https://doi.org/10.1080/21663831.2014.912690.
[6] C. Lee, et al., Lattice distortion in a strong and ductile refractory high-entropy alloy, Acta Mater. 160 (2018) 158–172, https://doi.org/10.1016/j.actamat.2018.08.053.
[7] Gao, M.C., et al., High-Entropy Alloys. 2016: Springer DOI:https://doi.org/10.1007/978-3-319-27013-5.
[8] J. Čížek, et al., Characterization of lattice distortions in refractory metal complex concentrated alloys using positron annihilation spectroscopy, Materialia (2022) 23, https://doi.org/10.1016/j.mtla.2022.101450.
[9] J. Málek, et al., Microstructure and mechanical properties of sintered and heat-treated HfNbTaTiZr high entropy alloy, Metals 9 (12) (2019), https://doi.org/10.3390/met9121324.
[10] W. Li, P. Liu, P.K. Liaw, Microstructures and properties of high-entropy alloy films and coatings: a review, Mater. Res. Lett. 6 (4) (2018) 199–229, https://doi.org/10.1080/21663831.2018.1434248.
[11] P. Ren, et al., Sputter-deposited TiVCrZrW high entropy alloy film: structure and tribological properties, Ceram. Int. 48 (24) (2022) 37383–37393, https://doi.org/10.1016/j.ceramint.2022.09.005.
[12] N.I. Muhammad Nadzri, et al., High-entropy alloy for thin film application: a review, Coatings 12 (12) (2022), https://doi.org/10.3390/coatings12121842.
[13] Y. Qiu, et al., Corrosion of high entropy alloys, npj Mater. Degrad. 1 (1) (2017), https://doi.org/10.1038/s41529-017-0009-y.
[14] Y. Shi, B. Yang, P. Liaw, Corrosion-Resistant High-Entropy Alloys: A Review, Metals 7 (2017) 2, https://doi.org/10.3390/met7020043.
[15] H. Cheng, et al., Review—corrosion-resistant high-entropy alloy coatings: a review, J. Electrochem. Soc. 168 (11) (2021), https://doi.org/10.1149/1945-7111/ac34d0.
[16] P. Hruška, et al., Oxidation of amorphous HfNbTaTiZr high entropy alloy thin films prepared by DC magnetron sputtering, J. Alloys Compd. (2021) 869, https://doi.org/10.1016/j.jallcom.2020.157978.
[17] O.N. Senkov, et al., Microstructure and elevated temperature properties of a refractory TaNbHfZrTi alloy, J. Mater. Sci. 47 (9) (2012) 4062–4074, https://doi.org/10.1007/s10853-012-6260-2.
[18] D.-C. Tsai, et al., Oxidation resistance and structural evolution of (TiVCrZrHf)N coatings, Thin Solid Films 544 (2013) 580–587, https://doi.org/10.1016/j.tsf.2012.12.064.
[19] J. Mayandi, et al., High entropy alloy CrFeNiCoCu sputter deposited films: structure, electrical properties, and oxidation, J. Vac. Sci. Technol. A 40 (2) (2022), https://doi.org/10.1116/6.0001394.
[20] C. Wang, et al., The resistivity–temperature behavior of Al CoCrFeNi high-entropy alloy films, Thin Solid Films (2020) 700, https://doi.org/10.1016/j.tsf.2020.137895.
[21] X. Zhang, et al., Preparation and characterization of high-entropy alloy (TaNb)1−x (ZrHfTi)x superconducting films, Phys. Rev. Res. 2 (1) (2020), https://doi.org/10.1103/PhysRevResearch.2.013375.
[22] M. Sahlberg, et al., Superior hydrogen storage in high entropy alloys, Sci. Rep. 6 (2016) 36770, https://doi.org/10.1038/srep36770.
[23] C. Zlotea, et al., Hydrogen sorption in TiZrNbHfTa high entropy alloy, J. Alloys Compd. 775 (2019) 667–674, https://doi.org/10.1016/j.jallcom.2018.10.108.
[24] O. El-Atwani, et al., Outstanding radiation resistance of tungsten-based high-entropy alloys, Sci. Adv. 5 (3) (2019) eaav2002, https://doi.org/10.1126/sciadv.aav2002.
[25] X.H. Yan, et al., A brief review of high-entropy films, Mater. Chem. Phys. 210 (2018) 12–19, https://doi.org/10.1016/j.matchemphys.2017.07.078.
[26] O.N. Senkov, et al., Microstructure and room temperature properties of a high-entropy TaNbHfZrTi alloy, J. Alloys Compd. 509 (20) (2011) 6043–6048, https://doi.org/10.1016/j.jallcom.2011.02.171.
[27] F. Lukac, et al., Spark plasma sintering of gas atomized high-entropy alloy HfNbTaTiZr, J. Mater. Res. 33 (19) (2018) 3247–3257, https://doi.org/10.1557/jmr.2018.320.
[28] M. El Garah, P. Briois, F. Sanchette, Recent Progress on high-entropy films deposited by magnetron sputtering, Crystals 12 (3) (2022), https://doi.org/10.3390/cryst12030335.
[29] C.-W. Tsai, et al., Strong amorphization of high-entropy AlBCrSiTi nitride film, Thin Solid Films 520 (7) (2012) 2613–2618, https://doi.org/10.1016/j.tsf.2011.11.025.
[30] W. Sheng, et al., Nano-crystallization of high-entropy amorphous NbTiAlSiWxNy films prepared by magnetron sputtering, Entropy 18 (6) (2016), https://doi.org/10.3390/e18060226.
[31] W.-J. Sheng, et al., Amorphous phase stability of NbTiAlSiNx high-entropy films, Rare Metals 37 (8) (2017) 682–689, https://doi.org/10.1007/s12598-016-0840-2.
[32] B.R. Braeckman, D. Depla, On the amorphous nature of sputtered thin film alloys, Acta Mater. 109 (2016) 323–329, https://doi.org/10.1016/j.actamat.2016.02.035.
[33] A. Xia, R. Franz, Thermal stability of MoNbTaVW high entropy alloy thin films, Coatings 10 (10) (2020), https://doi.org/10.3390/coatings10100941.
[34] B.R. Braeckman, D. Depla, Structure formation and properties of sputter deposited Nbx-CoCrCuFeNi high entropy alloy thin films, J. Alloys Compd. 646 (2015) 810–815, https://doi.org/10.1016/j.jallcom.2015.06.097.
[35] M.D. Cropper, Thin films of AlCrFeCoNiCu high-entropy alloy by pulsed laser deposition, Appl. Surf. Sci. 455 (2018) 153–159, https://doi.org/10.1016/j.apsusc.2018.05.172.
[36] H.-d. Wang, et al., Microstructure and corrosion behaviour of AlCoFeNiTiZr high-entropy alloy films, Surf. Eng. 36 (1) (2019) 78–85, https://doi.org/10.1080/02670844.2019.1625127.
[37] E.A. Laszlo, et al., Characteristics of thin high entropy alloy films grown by pulsed laser deposition, Coatings 12 (8) (2022), https://doi.org/10.3390/coatings12081211.
[38] J. Čížek, et al., Strength enhancement of high entropy alloy HfNbTaTiZr by severe plastic deformation, J. Alloys Compd. 768 (2018) 924–937, https://doi.org/10.1016/j.jallcom.2018.07.319.
[39] D.E. Jodi, et al., Study of vacancies in Fe (CoCrMnNi)100- medium- and high-entropy alloys by positron annihilation spectroscopy, Scr. Mater. (2021) 194, https://doi.org/10.1016/j.scriptamat.2020.113654.
[40] J. Čížek, T. Vlasák, O. Melikhova, Characterization of lattice defects in refractory metal high-entropy alloy HfNbTaTiZr by means of positron annihilation spectroscopy, Phys. Status Solidi A (2022), https://doi.org/10.1002/pssa.202100840.
[41] H. Guo, et al., Growth of nanoporous high-entropy oxide thin films by pulsed laser deposition, J. Mater. Res. 37 (1) (2022) 124–135, https://doi.org/10.1557/s43578-021-00473-2.
[42] P. Zhang, et al., Recent progress on the microstructure and properties of high entropy alloy coatings prepared by laser processing technology: a review, J. Manuf. Process. 76 (2022) 397–411, https://doi.org/10.1016/j.jmapro.2022.02.006.
[43] Y. Xu, et al., Solid-state cold spraying of FeCoCrNiMn high-entropy alloy: an insight into microstructure evolution and oxidation behavior at 700-900 °C, J. Mater. Sci. Technol. 68 (2021) 172–183, https://doi.org/10.1016/j.jmst.2020.06.041.
[44] C.-Z. Yao, et al., Electrochemical preparation and magnetic study of bi–Fe–co–Ni–Mn high entropy alloy, Electrochim. Acta 53 (28) (2008) 8359–8365, https://doi.org/10.1016/j.electacta.2008.06.036.
[45] C. Oses, C. Toher, S. Curtarolo, High-entropy ceramics, Nat. Rev. Mater. 5 (4) (2020) 295–309, https://doi.org/10.1038/s41578-019-0170-8.
[46] J.E. Berger, et al., Formation of self-ordered oxide nanotubes layer on the equiatomic TiNbZrHfTa high entropy alloy and bioactivation procedure, J. Alloys Compd. (2021) 865, https://doi.org/10.1016/j.jallcom.2021.158837.
[47] B. Schuh, et al., Thermodynamic instability of a nanocrystalline, single-phase TiZrNbHfTa alloy and its impact on the mechanical properties, Acta Mater. 142 (2018) 201–212, https://doi.org/10.1016/j.actamat.2017.09.035.
[48] J. Zýka, et al., Microstructure and room temperature mechanical properties of different 3 and 4 element medium entropy alloys from HfNbTaTiZr system, Entropy 21 (2) (2019), https://doi.org/10.3390/e21020114.
[49] G. Dirras, et al., Elastic and plastic properties of as-cast equimolar TiHfZrTaNb high-entropy alloy, Mater. Sci. Eng. A 654 (2016) 30–38, https://doi.org/10.1016/j.msea.2015.12.017.
[50] A. Motallebzadeh, et al., Mechanical properties of TiTaHfNbZr high-entropy alloy coatings deposited on NiTi shape memory alloy substrates, Metall. Mater. Trans. A 49 (6) (2018) 1992–1997, https://doi.org/10.1007/s11661-018-4605-4.
[51] X. Zhang, et al., Suppression of the transition to superconductivity in crystal/glass high-entropy alloy nanocomposites, Commun. Phys. 5 (1) (2022), https://doi.org/10.1038/s42005-022-01059-y.
[52] B.R. Braeckman, et al., High entropy alloy thin films deposited by magnetron sputtering of powder targets, Thin Solid Films 580 (2015) 71–76, https://doi.org/10.1016/j.tsf.2015.02.070.
[53] Y.S. Kim, et al., Investigation of structure and mechanical properties of TiZrHfNiCuCo high entropy alloy thin films synthesized by magnetron sputtering, J. Alloys Compd. 797 (2019) 834–841, https://doi.org/10.1016/j.jallcom.2019.05.043.

[54] C. Cheng, et al., Accelerated discovery of (TiZrHf)(x)(NbTa)(1-x) high-entropy alloys with superior thermal stability and a new crystallization mechanism, Adv. Mater. 36 (31) (2024) e2403632, https://doi.org/10.1002/adma.202403632.
[55] L. Backman, E.J. Opila, Thermodynamic assessment of the group IV, V and VI oxides for the design of oxidation resistant multi-principal component materials, J. Eur. Ceram. Soc. 39 (5) (2019) 1796–1802, https://doi.org/10.1016/j.jeurceramsoc.2018.11.004.
[56] L. Backman, et al., Part I: theoretical predictions of preferential oxidation in refractory high entropy materials, Acta Mater. 197 (2020) 20–27, https://doi.org/10.1016/j.actamat.2020.07.003.
[57] L. Backman, et al., Part II: experimental verification of computationally predicted preferential oxidation of refractory high entropy ultra-high temperature ceramics, Acta Mater. 197 (2020) 81–90, https://doi.org/10.1016/j.actamat.2020.07.004.
[58] T.-K. Tsao, et al., High temperature oxidation and corrosion properties of high entropy Superalloys, Entropy 18 (2) (2016), https://doi.org/10.3390/e18020062.
[59] Q. Zhou, et al., Corrosion behavior of Hf0.5Nb0.5Ta0.5Ti1.5Zr refractory high-entropy in aqueous chloride solutions, Electrochem. Commun. 98 (2019) 63–68, https://doi.org/10.1016/j.elecom.2018.11.009.
[60] S.K. Bachani, et al., Microstructural characterization, mechanical property and corrosion behavior of VNbMoTaWAl refractory high entropy alloy coatings: effect of Al content, Surf. Coat. Technol. (2020) 403, https://doi.org/10.1016/j.surfcoat.2020.126351.
[61] Y. Gao, et al., Electrochemical corrosion and high temperature hot corrosion behavior of NbTaTiV and CrNbTaTiV high entropy alloy, J. Mater. Res. Technol. 28 (2024) 216–234, https://doi.org/10.1016/j.jmrt.2023.11.247.
[62] J. Čížek, Characterization of lattice defects in metallic materials by positron annihilation spectroscopy: a review, J. Mater. Sci. Technol. 34 (4) (2018) 577–598, https://doi.org/10.1016/j.jmst.2017.11.050.
[63] P. Hautojärvi, Positrons in Solids. Topics in Current Physics, Springer-Verlag, Berlin Heidelberg, 1979, https://doi.org/10.1007/978-3-642-81316-0.
[64] Order or disorder, Nat. Mater. 22 (8) (2023) 925, https://doi.org/10.1038/s41563-023-01636-8.
[65] A. van Veen, et al., *Analysis of positron profiling data by means of "VEPFIT"* AIP Conference Proceedings 218, 1991, p. 171, https://doi.org/10.1063/1.40182.
[66] A. van Veen, et al., VEPFIT applied to depth profiling problems, Appl. Surf. Sci. 85 (1995) 216–224, https://doi.org/10.1016/0169-4332(94)00334-3.
[67] A.A. Coelho, TOPASandTOPAS-academic: an optimization program integrating computer algebra and crystallographic objects written in C++, J. Appl. Crystallogr. 51 (1) (2018) 210–218, https://doi.org/10.1107/s1600576718000183.
[68] Thermo-Calc Software. 1. 2, Available from: https://thermocalc.com/wp-content/uploads/Documentation/Databases/Thermodynamic/tchea7-technical-info.pdf, 2024.
[69] The XPS Library [cited 2024 2024/08/08]; Available from: https://xpslibrary.com/.
[70] The International XPS Database [cited 2024 2024/08/08]; Available from: https://xpsdatabase.net/.
[71] H. Schut, A Variable Energy Positron Beam Facility with Applications in Materials Science, 1990.
[72] P.J. Schultz, K.G. Lynn, Interaction of positron beams with surfaces, thin films, and interfaces, Rev. Mod. Phys. 60 (3) (1988) 701–779, https://doi.org/10.1103/RevModPhys.60.701.
[73] D. Ma, A.D. Stoica, X.L. Wang, Power-law scaling and fractal nature of medium-range order in metallic glasses, Nat. Mater. 8 (1) (2009) 30–34, https://doi.org/10.1038/nmat2340.
[74] N.N. Greenwood, A. Earnshaw, Chemistry of the Elements, 2nd ed., Elsevier, 1997, p. 1600, https://doi.org/10.1016/C2009-0-30414-6.
[75] R.P. R., Handbook of Corrosion Engineering 2 ed., Vol. 2012, McGraw-Hill, 2012.
[76] Watts, J.F. and J. Wolstenholme, An Introduction to Surface Analysis by XPS and AES. 2019: Wiley DOI:https://doi.org/10.1002/9781119417651.
[77] M.A. Baker, et al., Femtosecond laser ablation (fs-LA) XPS – a novel XPS depth profiling technique for thin films, coatings and multi-layered structures, Appl. Surf. Sci. (2024) 654, https://doi.org/10.1016/j.apsusc.2024.159405.
[78] A. Pundt, R. Kirchheim, HYDROGEN IN METALS: Microstructural Aspects, Annu. Rev. Mater. Res. 36 (1) (2006) 555–608, https://doi.org/10.1146/annurev.matsci.36.090804.094451.
[79] R. Kirchheim, Hydrogen solubility and diffusivity in defective and amorphous metals, Prog. Mater. Sci. 32 (4) (1988) 261–325, https://doi.org/10.1016/0079-6425(88)90010-2.